CHARACTERIZING $GE_{28}SB_{12}SE_{60}$ IN THE NEAR- AND MID-INFRARED

by

CAROLINE LOCKHART HUGHES

A thesis submitted in partial fulfillment of the requirements for graduation with

Honors from the Department of Physics

EXAMINING COMMITTEE

Professor Juliet Gopinath, Thesis Advisor
Departments of Physics and Electrical, Computer, and Energy Engineering

Professor John Cumulat, Honors Council Representative
Department of Physics

Professor Wounjhang Park
Department of Electrical, Computer, and Energy Engineering

Professor Thomas Schibli
Department of Physics

UNIVERSITY OF COLORADO BOULDER

APRIL 30, 2015

This thesis entitled:
Characterizing $Ge_{28}Sb_{12}Se_{60}$ in the Near- and Mid-Infrared
written by Caroline Lockhart Hughes
has been approved for the Department of Physics

Professor Juliet Gopinath

Professor John Cumulat

Professor Wounjhang Park

Professor Thomas Schibli

Date

The final copy of this thesis has been examined by the signatories, and we find that both the content and the form meet acceptable presentation standards of scholarly work in the above mentioned discipline.

Hughes, Caroline Lockhart (B.S., Engineering Physics)

Characterizing $Ge_{28}Sb_{12}Se_{60}$ in the Near- and Mid-Infrared

Thesis directed by Professor Juliet Gopinath

This thesis examines applications of chalcogenide glasses and their potential for use in the mid-infrared region and discusses methods by which the bulk loss absorption of these materials can be measured in this regime. The bulk loss was measured for $Ge_{28}Sb_{12}Se_{60}$ as well as reference sample $Ge_{33}As_{12}Se_{55}$ in both the near- and mid-infrared, at specific wavelengths of 1.534 µm and 3.677 µm. The bulk loss for the $Ge_{28}Sb_{12}Se_{60}$ sample was measured to be $(0.07 \pm 0.20)\,\mathrm{cm}^{-1}$ in the near-infrared and $(0.06 \pm 0.18)\,\mathrm{cm}^{-1}$ in the mid-infrared. This value was measured for the $Ge_{33}As_{12}Se_{55}$ reference sample to be $(0.07 \pm 0.20)\,\mathrm{cm}^{-1}$ in the near-infrared and $(0.03 \pm 0.16)\,\mathrm{cm}^{-1}$ in the mid-infrared. The expected values of bulk loss, calculated using values of extinction coefficients listed on the Refractive Index Database, were $0.059\,\mathrm{cm}^{-1}$ at 1.534 µm and $0.048\,\mathrm{cm}^{-1}$ at 3.677 µm for the $Ge_{28}Sb_{12}Se_{60}$ sample and $0.036\,\mathrm{cm}^{-1}$ at 1.534 µm and $0.028\,\mathrm{cm}^{-1}$ at 3.677 µm for the $Ge_{33}As_{12}Se_{55}$ reference sample. The approximate agreement with expected values, suggests that these measurements provide good order-of-magnitude estimates of the bulk loss values of the two materials, limited by the large error on the approximations. Ultimately, this suggests that both $Ge_{28}Sb_{12}Se_{60}$ and $Ge_{33}As_{12}Se_{55}$ can be considered transparent in the infrared.

DEDICATION

To my grandparents,

Joyce, Janet, and Jim

ACKNOWLEDGEMENTS

I would first and foremost like to thank Professor Juliet Gopinath and Molly Krogstad, for their extraordinary patience, encouragement, and guidance throughout the duration of this project. I would also like to thank Kenneth Underwood, Robert Niederriter, Kevin Dease, and Trystan Binkley-Jones for their advice and support.

Thank you Dr. Todd Rosenfeld for inspiring and encouraging my scientific curiosity through Astronomy at Centennial High School. Finally, I would like to thank my family, Mom, Dad, and Andrea, for your love and support.

CONTENTS

TABLES

Table

FIGURES

Figure

CHAPTER I

BACKGROUND

Chalcogenides are nonlinear materials that have excellent potential to be used in novel optical devices. These glasses contain at least one chalcogen element, specifically sulfur, selenium, or tellurium, as well as "more electropositive elements," such as arsenic or germanium [2, 3]. Chalcogenide glasses are particularly enticing because they are transparent in the infrared, creating new possibilities of fabricating optical devices for this regime. The (3-5) µm range has excellent potential for use in optical sensing, although research concerning the properties of chalcogenides exposed to these wavelengths of light is still in its early stages [1, 4]. Two optical properties are particularly important to consider when assessing possible applications and uses of these glasses: bulk loss and nonlinearity. Nonlinearity refers to the change in the refractive index of a material in the presence of an electric field. A material's linear absorption, described by its bulk loss coefficient α, corresponds with the amount of light that is effectively lost in the sample and cannot benefit from the effects of the nonlinearity.

Infrared Spectroscopy for Materials Sensing

Light in the infrared region, particularly between (2-10) µm, has incredible potential for use in chemical sensing [7]. Molecular bonds vibrate with resonant frequencies, and when they are exposed to light with the same frequency, the molecule can absorb energy from this light. The

"fingerprint" region, for example, specifically describes the stretching of C—C, C—O, and C—N bonds. The strength of the bonds, masses of the atoms in the bonds, and types of vibrations determine the position of the absorption in the infrared spectrum [8]. Therefore, measuring this absorption can provide a lot of information about many ubiquitous materials.

The HITRAM Molecular Spectroscopic Database catalogs spectroscopic data, including absorption cross-section, for molecules [6]. Willer et al. used data from the 2004 Database to calculate and plot absorption envelopes for seven common molecules: water, carbon monoxide, nitrogen dioxide, nitrogen monoxide, carbon dioxide, sulfur dioxide, and hydrogen sulfide. This plot for wavelengths ranging from (1-7) µm is included in Figure 1 [5].

Stronger bonds absorb at higher wavelengths, making it impossible to analyze these materials without light sources in the mid-infrared region [8]. However, few light sources and optical devices exist for this regime.

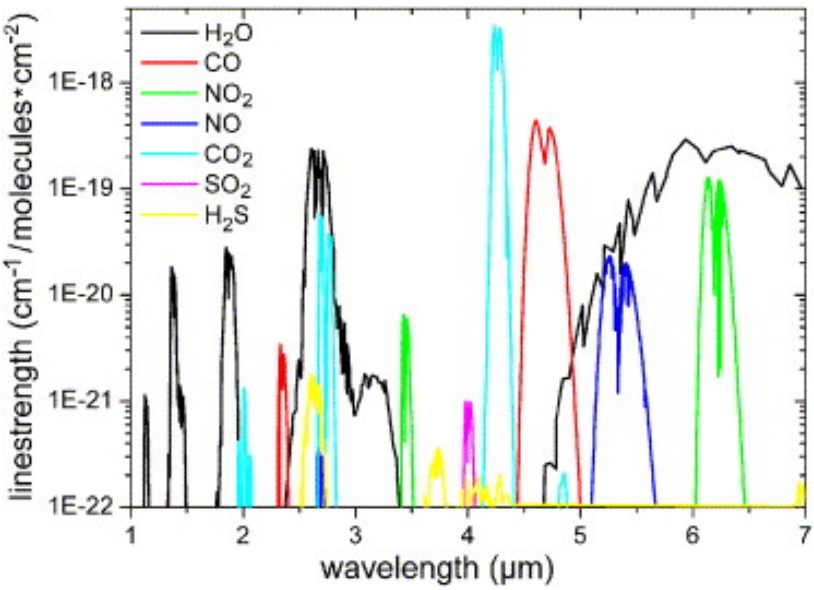

Figure 1: Absorption Bands in the Chemical Fingerprint Region

This plot shows the absorption bands of seven common molecules in the chemical fingerprint region using data from the HITRAN 2004 Database [5, 6].

Chalcogenide Glasses

The material of interest, $Ge_{28}Sb_{12}Se_{60}$, which is fabricated by doping GeSe with Sb, has the benefit of being arsenic-free, making it less hazardous than other chalcogenides, such as As_2Se_3 [9]. More interestingly, the band gap falls in the visible to near-infrared region, meaning that chalcogenides are transparent in the infrared regime [2]. Furthermore, the high nonlinearity of these materials make them excellent candidates for use in applications including spectral broadening and ultrafast optical switching [4, 10]. Both of these effects have been observed in chalcogenide As_2S_3, which is both low-loss and highly nonlinear [11, 12]. Similar qualities are expected in $Ge_{28}Sb_{12}Se_{60}$; however, it is important to examine the nonlinearity and loss of this material to determine the practicality of using this glass in the fabrication of nonlinear optical devices.

High Nonlinearity

Nonlinearity occurs when a material's polarization, $\vec{P}$, changes in the presence of an electric field, $\vec{E}$, such that the displacement field, $\vec{D}$, cannot be written as a linear combination of the polarization and electric fields [13]. For a nonlinear system, $\vec{P}(t)$ can be computed as a power series expansion in $\vec{E}(t)$. The first terms of this series are given in Equation 1 [14].

$$\vec{P}(t) = \chi^{(1)}\vec{E}(t) + \chi^{(2)}\vec{E}^{(2)}(t) + \chi^{(3)}\vec{E}^{(3)}(t) + \dots \tag{1}$$

Where $\chi^{(1)}$ is the linear susceptibility tensor, which makes sense since, for a linear material, polarization and electric field are related by the first term in the expansion [13]. For a nonlinear system, $\chi^{(2)}$ and $\chi^{(3)}$ are the second- and third-order susceptibilities [14]. Even-ordered susceptibility tensors, here $\chi^{(2)}$, are zero for isotropic materials, including amorphous solids such as chalcogenide glasses [15]. For this reason, the $\chi^{(2)}$ term was not considered. $\chi^{(3)}$, the third-order susceptibility, describes the nonlinearity of the material.

Like polarization, the index of refraction of a nonlinear material also changes in the presence of an electric field. The nonlinear index is given in Equation 2, where n_0 is the usual refractive index, n_2 is the nonlinear index, and I is the intensity of the electric field incident on the sample, averaged over time [16].

$$n = n_0 + n_2 I \tag{2}$$

This is also referred to as the Kerr effect. It is "proportional to the real part of the third-order nonlinear susceptibility $\chi^{(3)}$" [17]. This relationship is stated explicitly in Equation 3, where n_0 is the linear refractive index, ϵ_0 is the permittivity of free space, and c is the speed of light in a vacuum [16].

$$n_2 \left[\mathrm{m}^2/\mathrm{W}\right] = \frac{3}{4n_0^2\epsilon_0 c}\chi^{(3)} \left[\mathrm{m}^2/\mathrm{V}^2\right] = \frac{283}{n_0^2}\chi^{(3)} \left[\mathrm{m}^2/\mathrm{V}^2\right] \tag{3}$$

The theoretical wavelength-dependent nonlinear index inside a material, can be found using Equation 4, which was described by Lenz et al [9]:

$$n_2(\lambda) = \left(1.7 \times 10^{-14}\right)\left(n_0^2 + 2\right)^3\left(n_0^2 - 1\right)\left(\frac{d}{n_0 E_s}\right)^2 F\left(x\right)\ \mathrm{cm}^2/\mathrm{W} \tag{4}$$

$$\text{where } x = \frac{\hbar\omega}{E_g} = \frac{hc}{\lambda E_g}$$

Where $h = 2\pi\hbar$ is Planck's constant, c is the speed of light in a vacuum, d is the "mean cation-anion bond length of the bonds that are primarily responsible for the nonlinear response," E_g is the optical or Tauc gap, and E_s is the Sellmeier gap [17, 9]. The optical gap is "the energy at which the absorption changes from a parabolic density of states to a Urbach tail absorption" and the Sellmeier gap is the "average valence-conduction band energy, weighted by the strength of the virtual excitations contributing to the optical response" [9]. For $Ge_{28}Sb_{12}Se_{60}$, $d = 0.251\,\mathrm{nm}$, $E_g = 1.8\,\mathrm{eV}$, and $E_s = 4.14\,\mathrm{eV}$ [9].

The function $F(x)$, where x is the ratio of photon energy, $\hbar\omega$, to E_g, depends on the four

phenomena that can contribute to nonlinearity: two-photon absorption, raman scattering, and the linear and quadratic Stark Effects [18]. Each term in $F(x)$ is listed in Appendix C for convenience. This term is plotted for $0 < x < 1$ in Figure 2a. The refractive index referenced in Equation 4 is also a function of wavelength. Figure 2b shows the plot of n_0 for $Ge_{28}Sb_{12}Se_{60}$ as a function of wavelength from (1-4) µm [19].

With this information, it is now possible to plot the nonlinear refractive index, n_2 as a function of wavelength over the same range. This is shown for $Ge_{28}Sb_{12}Se_{60}$ in Figure 3. Nonlinearity is maximized at $\approx 1.287\,\mu m$. The nonlinearity of this particular chalcogenide material is significantly greater than that of non-chalcogenide nonlinear materials at 1.55 µm, fused silica and silicon, and greater than other chalcogenide materials, summarized in Table 1, which was compiled at by Professors Park and Gopinath [1].

Table 1: Measured Nonlinearity of Chalcogenides and Other Materials at 1.55 µm [1]
These materials are some of those compiled by Professors Park and Gopinath for an NSF proposal highlighting the benefits of using chalcogenides over fused silica and silicon.

Material	Nonlinearity $\left(10^{-20}\mathrm{m}^2/\mathrm{W}\right)$
Fused silica	2.6
Silicon	450
As_2S_3	1300
$Ge_{33}As_{12}Se_{55}$	1500
$Ge_{28}Sb_{12}Se_{60}$	936

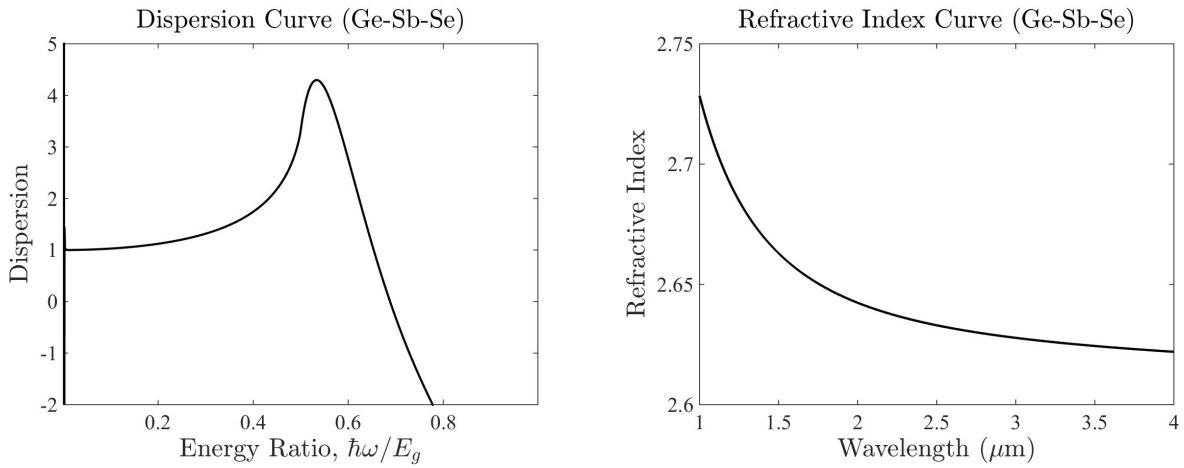

(a) Dispersion Curve, $F(x)$ **(b)** Refractive Index, n_0

Figure 2: Wavelength-Dependent Terms in the Nonlinear Refractive Index Function

These plots show the functions referenced when calculating the nonlinear refractive index (Equation 4) [9, 18]. Both dispersion and refractive index vary as a function of wavelength and are plotted here over (1-4) µm for the $Ge_{28}Sb_{12}Se_{60}$ sample.

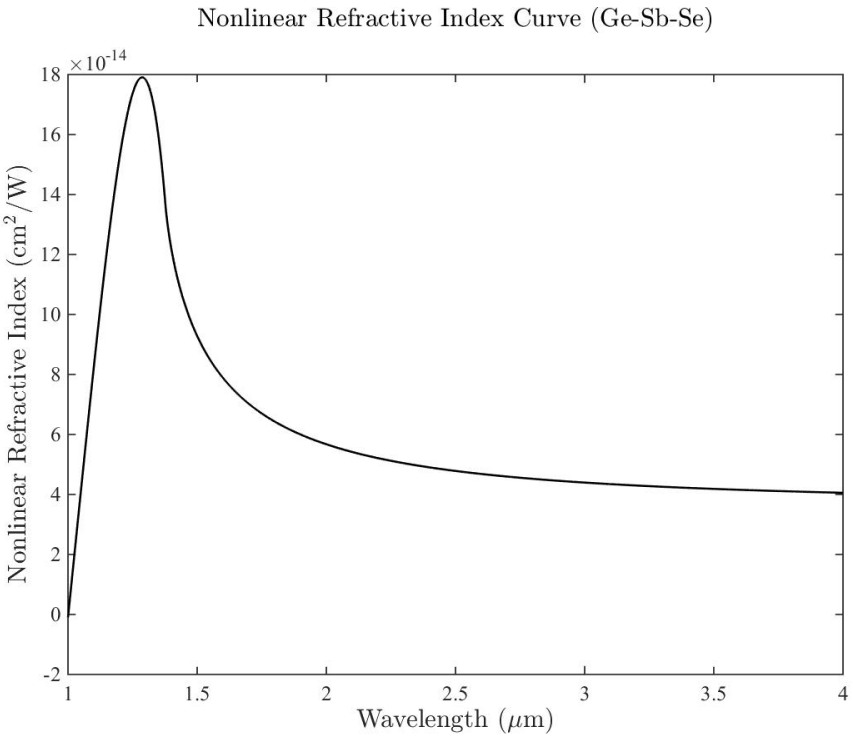

Figure 3: Nonlinear Refractive Index, n_2

This plot shows n_2 of the $Ge_{28}Sb_{12}Se_{60}$ sample, calculated using Equation 4.

Infrared Transparency

This work mainly focuses on quantifying the infrared transparency of $Ge_{28}Sb_{12}Se_{60}$ by measuring its bulk loss coefficient in both the near- and mid-infrared. Values have been estimated for samples with the same compositions that were manufactured by a different company, and are listed in Table 2.

Table 2: Summary of Expected Bulk Loss Coefficients

These values were estimated based on extinction coefficient (κ) values listed online by Polyanskiy on the Refractive Index Database [20, 21] which can be related to bulk loss using Equation 5.

Wavelength	$Ge_{33}As_{12}Se_{55}$	$Ge_{28}Sb_{12}Se_{60}$
1534.29 nm	$0.036\,\mathrm{cm}^{-1}$	$0.059\,\mathrm{cm}^{-1}$
3677.43 nm	$0.028\,\mathrm{cm}^{-1}$	$0.048\,\mathrm{cm}^{-1}$

This estimate was performed for each sample using the extinction coefficient κ, which is related to bulk loss, α, by Equation 5.

$$\alpha = \frac{4\pi\kappa}{\lambda} \tag{5}$$

The extinction coefficients and expected bulk loss coefficients are listed in Table 6, which, along with Table 5, summarizes all sample properties used in calculations.

It is important to note that these values of α are very small and measuring them requires careful experimental development and analysis. Two different techniques were carefully considered as possible methods of measuring this quantity. Detailed measurement analysis was completed before a method was ultimately selected and performed for both the near- and mid-infrared.

CHAPTER II

METHOD SELECTION

The measurements were completed for the near-infrared using the Brewster angle measurement technique, which is described in detail in this chapter. However, selecting the process by which the bulk loss coefficient would be measured in the mid-infrared presented several unique challenges. Most significantly, the measurement procedure would have to be very sensitive in order to detect the small bulk loss coefficient value expected. This was made more difficult by the limited light source options for the 3 µm range. Since 3 µm light is less-commonly used, as compared to 1.55 µm light, options of detectors that are sensitive in this regime are limited due to lower demand. The Thorlabs PDA20H lead selenide (PbSe) detector was considered when making calculations that would determine both which method to use and the expected uncertainty in the bulk loss coefficient.

Two different measurement techniques were considered, each taking advantage of basic physical principles and applying them to the linear absorption measurement: laser calorimetry and the Brewster angle. These methods were compared assuming 1 mW of power from the 3 µm optical parametric oscillators (OPO), which severely limited the sensitivity of the measurements and greatly influenced which technique was ultimately chosen to measure the bulk loss coefficients of $Ge_{33}As_{12}Se_{55}$ and $Ge_{28}Sb_{12}Se_{60}$.

Two major companies manufacture chalcogenide samples: SCHOTT and VITRON. SCHOTT IRG 22 and VITRON IG 2 have the same $Ge_{33}As_{12}Se_{55}$ composition and SCHOTT IRG 25 and VITRON IG 2 have the same $Ge_{28}Sb_{12}Se_{60}$ composition. The samples used in the lab are both manufactured by SCHOTT; however, data on the comparable VITRON samples proved useful

when conducting the method analysis. In particular, data on the extinction coefficient enabled direct calculation of the expected bulk loss coefficients of the two samples. All of the sample properties referenced are listed in Tables 5 and 6.

Laser Calorimetry Measurement Technique

The laser calorimetry measurement technique involves heating a sample for given time and measuring the rate of change in temperature of the sample with respect to time, $\Delta T/\Delta t$. The steady state differential temperature ΔT is the difference in temperature between the sample and a cooled reference sample, shown in Figure 4, measured with a differential thermocouple [22]. The sample would be heated for a time t_B, which is the bulk-heating thermal time constant of the sample. This describes the time it takes for the heat from the laser to reach every point within the bulk of the sample and can be calculated using Equation 6, where r is the sample radius, c_p is its specific heat, k_{Th} is thermal conductivity, κ_{Th} is thermal diffusivity, and ρ is density [22, 23].

$$t_B = \frac{r^2}{6\kappa_{Th}}, \qquad \kappa_{Th} = \frac{k_{Th}}{\rho c_p} \tag{6}$$

For the $Ge_{33}As_{12}Se_{55}$ and $Ge_{28}Sb_{12}Se_{60}$ samples, $t_B \approx 163\,\mathrm{s}$ and $t_B \approx 165\,\mathrm{s}$.

A plot of ΔT as a function of time should have a linear slope immediately after the laser has been turned on as the sample is heated over t_B. Since ΔT is the differential temperature, $\Delta T = 0$ at $t = 0$ and ΔT should be the steady-state differential temperature at t_B. This slope can be used to calculate the bulk loss of the sample, where P is the laser power and L is the sample thickness [22, 24]:

$$\alpha = \frac{mc_p}{PL}\frac{\Delta T}{t_B} \tag{7}$$

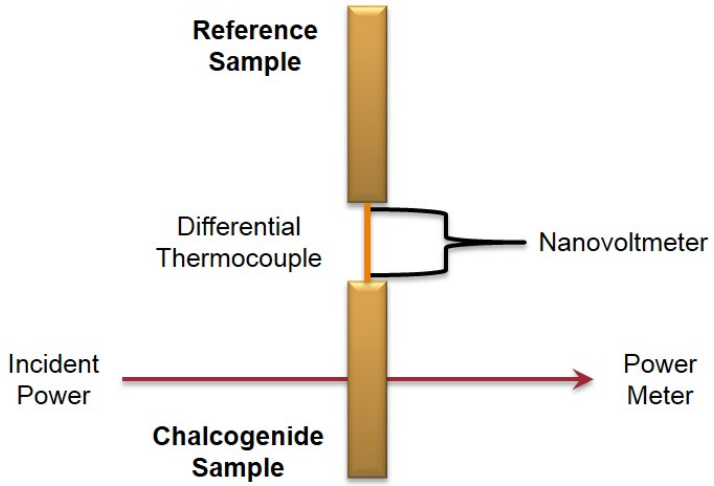

Figure 4: Laser Calorimetry Measurement Schematic

This diagram shows the basic schematic for the laser calorimetry measurement technique [22]. A laser incident on the sample heats it as the difference in temperature between the heated sample and a reference sample is monitored with a differential thermocouple and measured using a nanovoltmeter.

Pinnow and Rich suggest that a differential temperature of $\Delta T \approx 0.5\,^{\circ}\mathrm{C}$ could reasonably be measured [24], so this is the value used in order to determine whether the laser calorimetry technique could be a feasible means of measuring the bulk loss coefficient of the sample. This value of ΔT, $\Delta t = t_B$, $P = 1\,\mathrm{mW}$, and m, c_p, and L for $Ge_{33}As_{12}Se_{55}$ and $Ge_{28}Sb_{12}Se_{60}$ (listed in Table 5), the lowest-possible bulk loss coefficients that could be measured are:

$$\alpha = 22.6195\,\mathrm{cm}^{-1} \qquad (Ge_{33}As_{12}Se_{55})$$

$$\alpha = 23.5619\,\mathrm{cm}^{-1} \qquad (Ge_{28}Sb_{12}Se_{60})$$

These values are three orders of magnitude larger than the expected bulk loss coefficients listed in Table 6. Improving this measurement would require drastically increasing the OPO power and the differential temperature that could be measured by the differential thermocouples. Such challenges make this method infeasible, making the Brewster angle method a more attractive option.

Brewster Angle Measurement Technique

For all materials, there exists an angle θ_B, called the Brewster angle, at which the p-polarized light reflected from the surface of the material is minimized [13]. This angle, indicated in Figure 5. Can be calculated using Equation 8, where n_0 is the sample's refractive index.

$$n_0 = \tan\theta_B \tag{8}$$

This comes from two of the boundary conditions imposed by Maxwell's Equations [13]:

$$\left(\tilde{\vec{E}}_{0I} + \tilde{\vec{E}}_{0R}\right)^{\parallel} = \tilde{\vec{E}}^{\parallel}_{0T} \tag{9a}$$

$$\frac{1}{\mu_I}\left(\tilde{\vec{B}}_{0I} + \tilde{\vec{B}}_{0R}\right)^{\perp} = \frac{1}{\mu_T}\tilde{\vec{B}}^{\perp}_{0T} \tag{9b}$$

Where $\tilde{\vec{E}}$ and $\tilde{\vec{B}}$ are the complex electric and magnetic fields, and μ_I and μ_T are the permeability constants of the material in the regions before and after the interface. Figure 6 shows each of these fields as well as $\vec{k}$ in the direction of the Poynting vector for each wave.

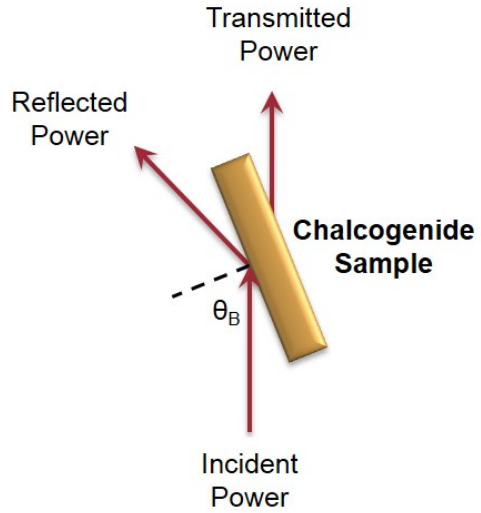

Figure 5: Brewster Angle Measurement Schematic
This diagram shows the basic schematic for the Brewster angle measurement technique, where θ_B is the angle at which the input beam is incident on the sample.

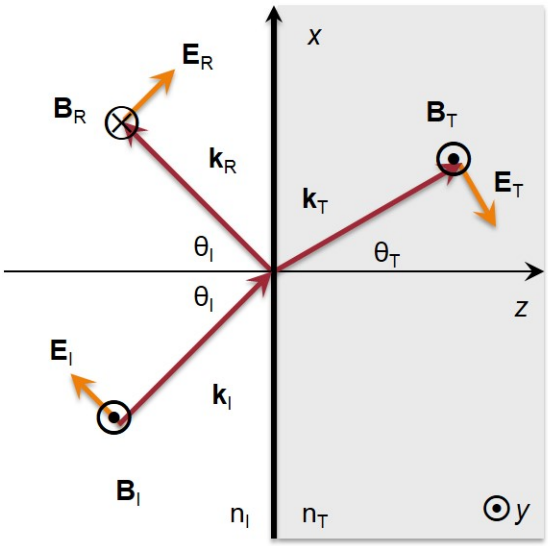

Figure 6: Snell's Law

This figure shows the electric and magnetic field vectors associated with the incident, reflected, and transmitted beams, each moving in the direction $\vec{k}_I$, $\vec{k}_R$, and $\vec{k}_T$, respectively.

For absorbing materials, the Brewster angle becomes that at which the reflectance, R, is minimized, rather than that at which $R = 0$. This adds a complex term to the index of refraction:

$$\tilde{n}_0 = n_0 + \imath\kappa \tag{10}$$

The relationship between θ_B and n_0 in Equation 8 assumes that the material has an entirely real index of refraction. However, since minimal absorption is expected for $Ge_{28}Sb_{12}Se_{60}$ in the mid-IR, the extinction coefficient, κ, should be very small, making the approximation in Equation 8 valid.

The reflectance and transmittance measured at the Brewster angle can be used to calculate the bulk loss coefficient of a nonlinear material [25]. In general, the reflectance R and transmittance T for a glass with a p-polarized incident beam near the Brewster angle are given by Equations 11a and 11b, where α is the bulk loss coefficient, L is the sample thickness, and $R_0 = r_p r_p^*$ is the reflectance at the surface of the glass [25].

$$R(\theta) = R_0 + \frac{(1 - R_0)^2 R_0 \exp\left(-2\alpha L/\cos\theta_T\right)}{1 - R_0^2 \exp\left(-2\alpha L/\cos\theta_T\right)} \tag{11a}$$

$$T(\theta) = \frac{(1 - R_0)^2 \exp\left(-\alpha L/\cos\theta_T\right)}{1 - R_0^2 \exp\left(-2\alpha L/\cos\theta_T\right)} \tag{11b}$$

The angle of refraction θ_T is found using Snell's Law (Equation 12), where θ_I and θ_T are the angles of incidence and refraction, depicted, along with the angle of reflection θ_R, in Figure 6, for a light passing from a material with refractive index n_I to one with refractive index n_T.

$$n_I \sin\theta_I = n_T \sin\theta_T \tag{12}$$

For angles near the Brewster angle, the measured reflectance should be minimized to R_{min} and transmittance should be maximized to T_{max}. Furthermore, the angle of refraction $\theta_{TB} = \pi/2 - \theta_B$ when $\theta_I = \theta_B$. In this limit, Equations 11a and 11b become [25]:

$$R_{min} = R_0\big(1 + \exp\left(-2\alpha L/\sin\theta_B\right)\big) \cong 2R_0, \qquad \alpha L \ll 1 \tag{13a}$$

$$T_{max} = (1 - R_0)^2 \exp\left(-\alpha L/\sin\theta_B\right) \tag{13b}$$

The approximation $\alpha L \ll 1$ is considered valid since αL is on the order of 0.01.

For p-polarized light, the complex Fresnel amplitude, $r_p(\theta)$, is given by Equation 14a, where $\tilde{n}_T$ is the complex refractive index given in Equation 10 [26].

$$r_p(\theta_I, \theta_T) = \frac{n_I \cos\theta_T - \tilde{n}_T \cos\theta_I}{n_I \cos\theta_T + \tilde{n}_T \cos\theta_I} \tag{14a}$$

Using Snell's Law as well as $n_I = 1$ for the index of refraction of air, the Fresnel amplitude becomes that given in Equation 14b.

$$r_p(\theta_I) = \frac{\sqrt{\left(n_0^2 + \kappa^2\right) - \sin^2\theta_I} - \left(n_0^2 + \kappa^2\right)\cos\theta_I}{\sqrt{\left(n_0^2 + \kappa^2\right) - \sin^2\theta_I} + \left(n_0^2 + \kappa^2\right)\cos\theta_I} \tag{14b}$$

$$r_p(\theta_B) = \frac{\sin\theta_B - (n_0 + \imath\kappa)\cos\theta_B}{\sin\theta_B + (n_0 + \imath\kappa)\cos\theta_B} \tag{14c}$$

With this expression, it becomes possible to plot the reflectance (Equation 11a) and transmittance (Equation 11b) as functions of angle of incidence θ_I. It is important to note that this plot was created for the general values of R and T rather than R_{min} and T_{max}, which are only true at the

Brewster angle. These curves are shown for both $Ge_{33}As_{12}Se_{55}$ and $Ge_{28}Sb_{12}Se_{60}$ at λ =3.677 µm on $0° \leq \theta_I \leq 90°$ in Figure 7a. Figures 7b and 7c show the same curves "zoomed in" to R_{min} and T_{max}.

From Equations 13a and 13b, it is possible to find the bulk loss coefficient α in terms of θ_B, L, R_{min} and T_{max}.

$$\alpha = \frac{\sin\theta_B}{L} \ln\left(\frac{(2 - R_{min})^2}{4T_{max}}\right) \tag{15}$$

This is an improvement over the laser calorimetry method since the transmission is expected to be very close to the incident power, which is $\approx$ 15 mW in the near-infrared and 1 mW in the mid-infrared.

The bulk loss measurement can be simplified by approximating $R_{min} \approx 0$, meaning that Equation 15, used to find the bulk loss of the sample using the measured reflectance and transmittance, becomes Equation 16, where T_{max} is still the measured transmittance at the angle at which transmittance is maximized and reflectance is minimized.

$$\alpha = -\frac{\sin\theta_B}{L} \ln T_{max} \tag{16}$$

Even after making this simplification, there is expected to be large uncertainty in these measurements, depending on both the power measured and the detector sensitivity for each method. This will be addressed further in Chapters III and IV, which describe the measurement processes in detail for both the near- and mid-infrared.

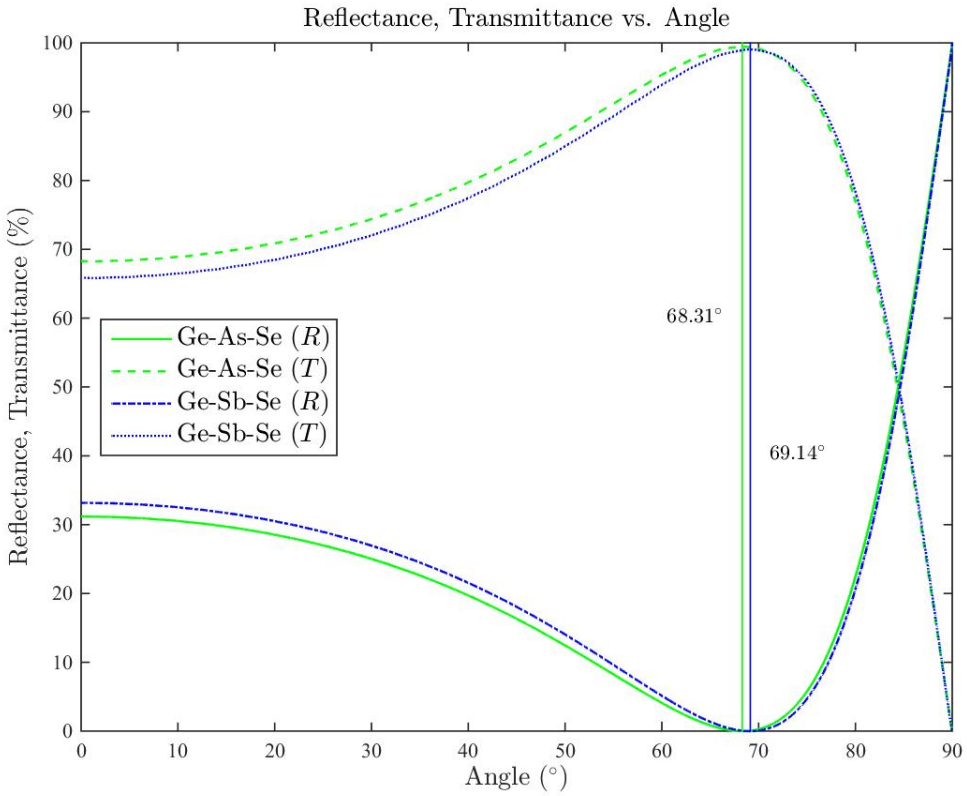

(a) Reflectance, Transmittance vs. Angle

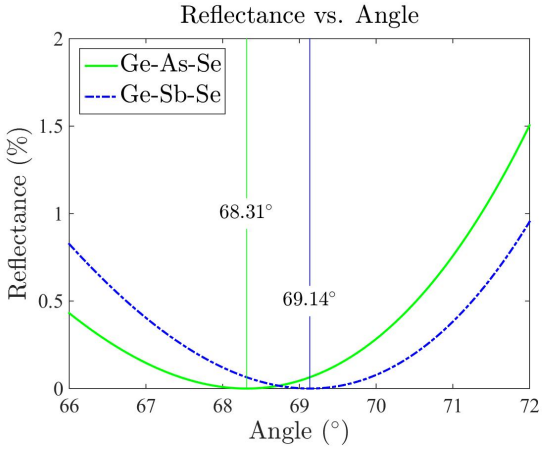

(b) Reflectance vs. Angle

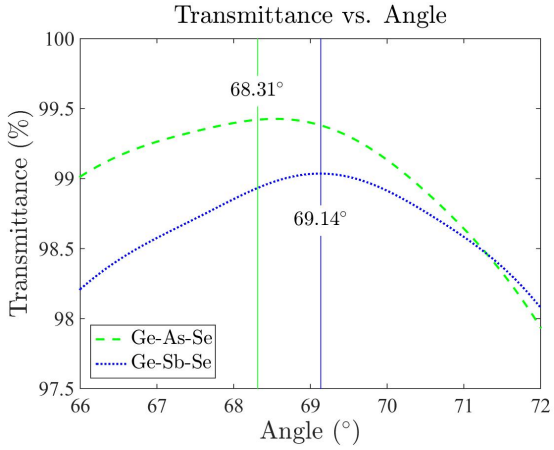

(c) Transmittance vs. Angle

Figure 7: Theoretical Reflectance and Transmittance Curves

These plots show the reflectance and transmittance curves, calculated using Equations 11a and 11b, for both the $Ge_{28}Sb_{12}Se_{60}$ and $Ge_{33}As_{12}Se_{55}$ samples, for the wavelength of the mid-infrared light ≈3.677 µm.

CHAPTER III

MEASURING THE BULK LOSS AT 1.534 µm

The bulk loss coefficients of the $Ge_{28}Sb_{12}Se_{60}$ and $Ge_{33}As_{12}Se_{55}$ samples were first measured in the near-infrared using an erbium fiber laser as a light source, constructed as a means to characterize chalcogenide waveguides.

Erbium Fiber Laser

The erbium fiber laser design was based on that described in the paper by Liu et al. [27], and is included in Figure 8 for reference. This design was chosen to measure the properties of chalcogenide waveguides near 1.55 µm. This laser design is flexible and can be mode-locked so that it emits pulses. For the purpose of the Brewster angle measurement, a pulsed laser was not necessary, but rather, operating at a continuous wavelength of 1.534 µm was adequate.

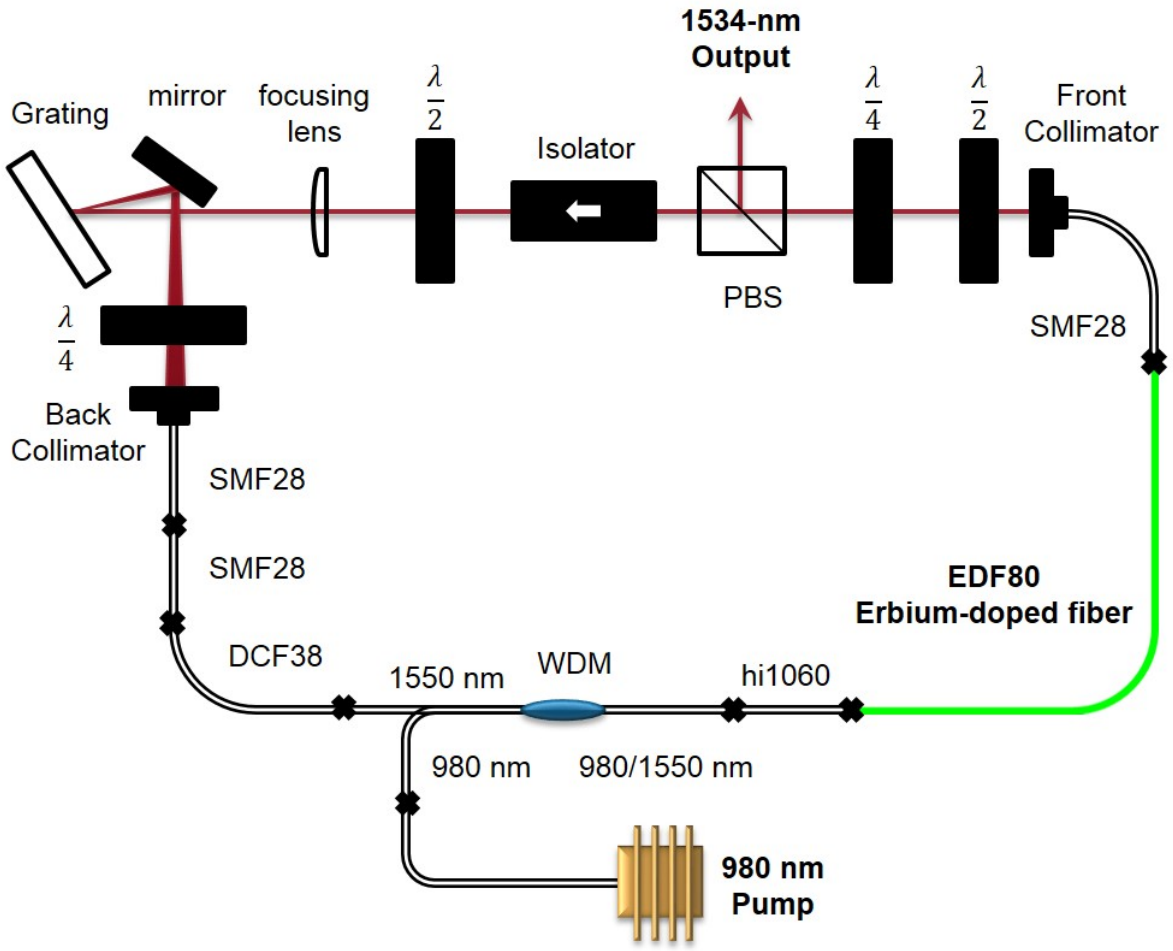

Figure 8: Erbium Fiber Laser Design

This figure shows the schematic for the erbium fiber laser at the time the bulk loss measurements were performed. The half waveplates (HWP) and quarter waveplates (QWP) were used to control the polarization of the light and thus the fraction of light that was transmitted or refracted by the polarizing beam splitter (PBS). Aside from erbium fiber, this set-up also contained single mode fiber (SMF), dispersion compensating fiber (DCF), as well as the hi1060 attached to the wavelength division multiplexer (WDM).

Experimental Design

Figure 9 shows the schematic for the Brewster angle measurement set-up. When measuring the bulk loss absorption using the Brewster Angle method, it was important first to verify on the

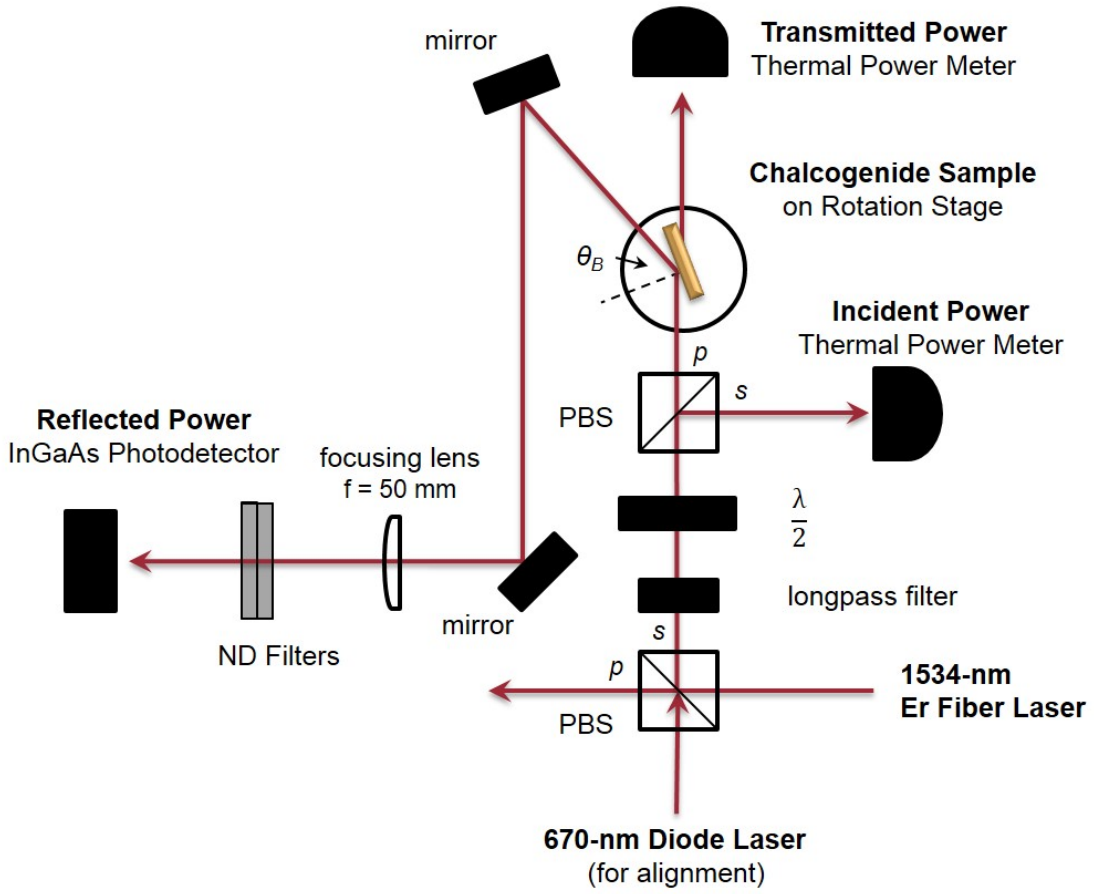

Figure 9: 1.534 µm Brewster Angle Measurement Set-Up

This figure shows the complete measurement set-up, including the erbium fiber laser light source, the 670 nm diode laser for alignment, and the optical components used to adjust the polarization of the 1.534 µm light and measure incident, transmitted, and reflected power. The chalcogenide sample is mounted on a rotation stage, which could be turned until the erbium fiber laser was incident on the sample at the Brewster angle, θ_B. The polarization of the light, p or s, is also indicated.

Optical Spectrum Analyzer that the 1.534 µm Er fiber laser was lasing. The spectrum typically resembled that shown in Figure 10, which was saved after the final absorption measurement had been taken. The longpass filter ensures that only 1.534 µm light is incident on the sample.

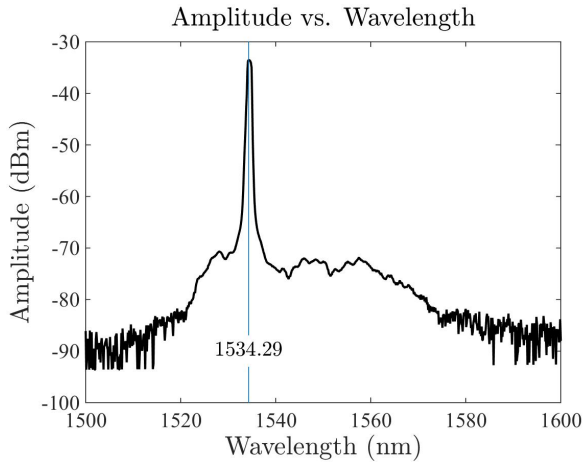

Figure 10: Erbium Fiber Laser Spectrum

This plot shows the erbium fiber laser spectrum measured on the Optical Spectrum Analyzer prior to taking the power measurements. The wavelength corresponding to the peak amplitude was used as the wavelength of light emitted by the erbium fiber laser.

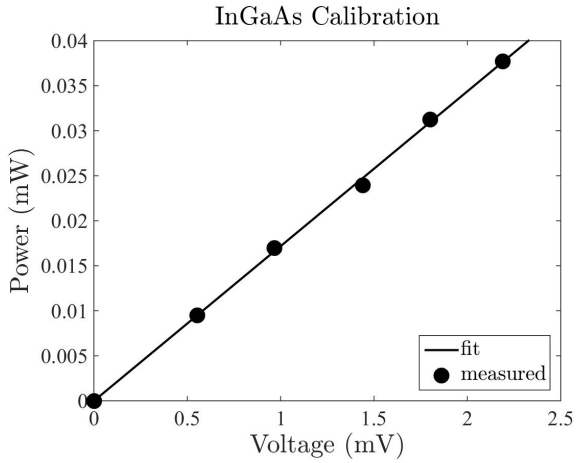

Figure 11: Photodetector Calibration

This plot shows relates the voltage measured on the InGaAs photodetector to an equivalent power in watts. This was determined by adjusting the current source for the laser and measuring the power on a thermal power meter and the voltage on the photodetector.

One of the biggest challenges in measuring the reflected power was that it was impossible to see the reflected beam. The 670 nm photodiode was used to align the Er fiber laser beam to the photodetector. It was important not to expose the chalcogenide samples to the 670 nm light for long periods of time, since this could lead to photo-darkening [28, 29]. The 670 nm diode laser was first aligned to the erbium fiber laser before placing the sample in the holder on the rotation stage. The diode laser was not turned back on again until after the sample was completely set-up for the measurement.

Setting up the sample involved calculating the Brewster angle θ_B based on the index of refraction for the sample. The sample was then placed in the holder on the rotation stage and positioned so that the incident beam from the erbium fiber laser is normal to the surface of the sample. This means that the beam reflected off the sample is either directly above or below the incident beam. Then the rotation stage was turned so that the sample was approximately at the

Brewster Angle, as shown in Figure 11. Then, it was possible to make very fine adjustments to the rotation of the sample while measuring the transmitted power. Maximum transmitted power will correspond with minimum reflected power [25].

At this point, the 670 nm diode laser was turned on and the mirrors were adjusted to align it through the focusing lens and to the photodiode detector measuring the reflected power. The diode laser was then turned off so that measurements could be made using the erbium fiber laser.

CHAPTER IV

MEASURING THE BULK LOSS AT 3.677 µm

The bulk loss coefficient was measured using the Brewster Angle measurement technique, selected after extensive method analysis performed in Chapter II. This measurement was completed using the ≈ 1 mW OPO in Professor Gopinath's lab. This measurement process is similar in theory to that followed to measure the bulk loss coefficient at 1.534 µm, although significant changes, including creative polarization optics, were made to address issues specific to working with light in the 3 µm range.

Optical Parametric Oscillator

Optical parametric oscillators are operated by exposing a nonlinear material to radiation in order to create an "induced polarization field" [30]. The nonlinearity of these materials is responsible for this effect, and their polarizations can, like those of chalcogenides, be described by Equation 1. In this case, however the $\chi^{(2)}$ term is what results in frequency generation. If two beams, with wavelengths λ_{pump} and λ_{signal}, are present, this can result in an "induced oscillating polarization" with frequency $\omega_{\text{idler}} = 2\pi/\lambda_{\text{idler}}$ [31]. A nonlinear material, in this case a fan-out periodically poled lithium niobate (PPLN) crystal, is used to create the two lower-energy beams with wavelengths of approximately $\lambda_{\text{signal}} \approx 1.5\,\mu\text{m}$ and $\lambda_{\text{idler}} \approx 3\,\mu\text{m}$, with nanosecond-pulses.

An Nd:YAG pump laser was used to generate the 3 µm light using an optical parametric oscillator (OPO). The singly resonant cavity was constructed as shown in Figure 14a to produce a signal and idler [31]. The amplitude of idler light at different wavelengths was measured and recorded for this OPO by Niederriter [32] and was plotted as shown in Figure 12. For this measurement, the crystal was located such that the three beams had the following wavelengths:

$$\lambda_{\text{pump}} = 1064.4\,\text{nm}$$

$$\lambda_{\text{signal}} = 1462.6\,\text{nm}$$

$$\lambda_{\text{idler}} = 3677.43\,\text{nm}$$

λ_{pump} and λ_{signal} could be measured directly using an optical spectrum analyzer. The wavelength of the idler, λ_{idler}, was then calculated using conservation of energy:

$$\frac{1}{\lambda_{\text{pump}}} = \frac{1}{\lambda_{\text{signal}}} + \frac{1}{\lambda_{\text{idler}}} \tag{17}$$

Figure 13 shows the OPO schematic. The isolator ensures that no power is reflected back into the pump, and the half-wave plate, designated "$\lambda/2$," and the polarizing beam splitter enable easy control over the pump power. The focusing lens is positioned such that the beam should be focused to a waist of $\approx 0.04\,\text{mm}$ at the PPLN crystal, so that all of the pump light passes through the crystal. The three steering mirrors are used to maneuver the beam to the crystal.

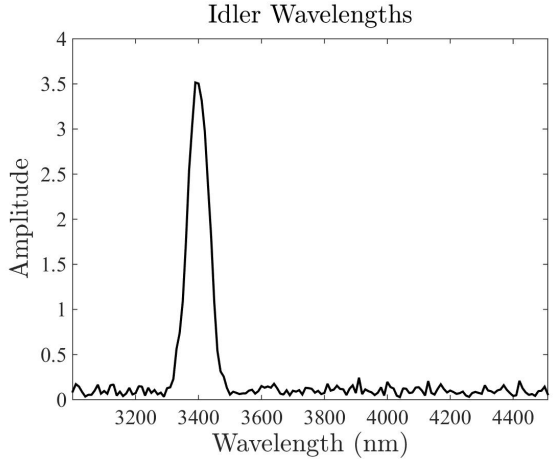

Figure 12: Idler Wavelengths

This plot shows the wavelengths of the idler that can be generated by moving the PPLN crystal translationally. This was measured by Niederriter for the OPO used to make the bulk loss measurements [32]

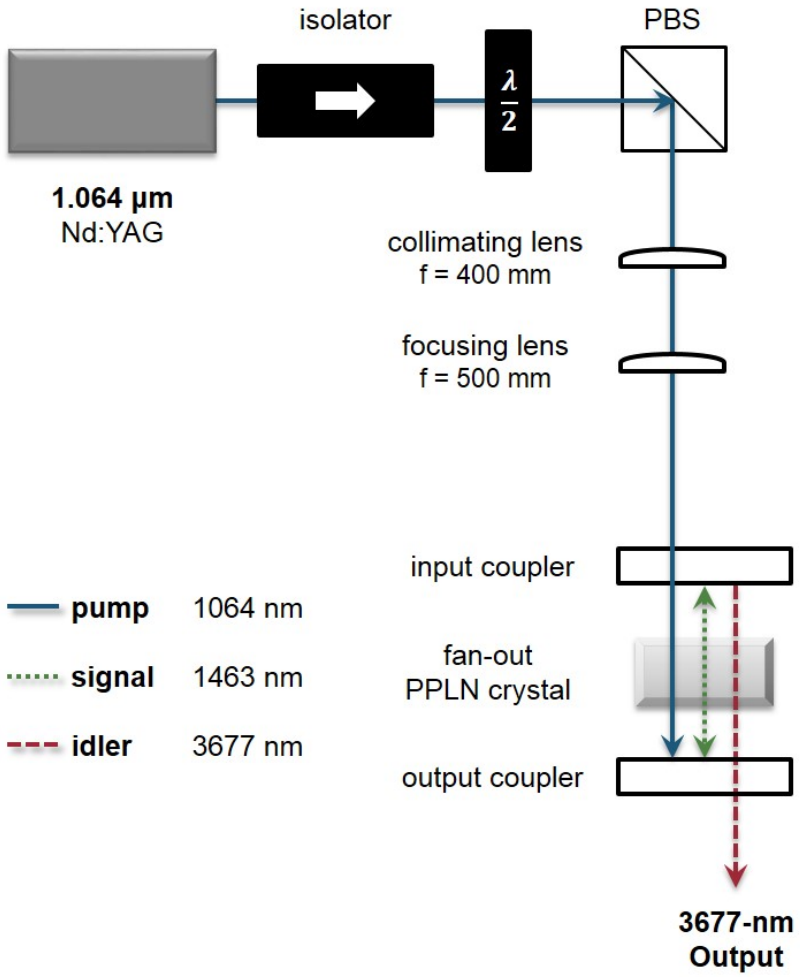

Figure 13: Optical Parametric Oscillator Schematic

This figure shows the complete OPO set-up. It begins with a 1 µm pump, followed by an isolator to ensure that no light can be reflected back into the pump. The half waveplate, labeled "$\lambda/2$" is used to adjust the polarization of the light which determines how much light is refracted by the polarizing beam splitter (PBS) and guided toward the fan-out periodically poled lithium niobate (PPLN) crystal.

After this set-up was complete, it was important to optimize the input and output couplers, which are the mirrors in Figure 14a. These are dichroic mirrors, which were chosen since only the 1 µm pump light was intended to be transmitted through the input coupler with the goal of producing 3 µm light. Using the output coupler to reflect the pump light back through the crystal also effectively created created "signal gain on both the forward and backward transits of the crystal" [33], helping to produce the signal and idler. The exact wavelengths of the signal and

idler could be adjusted by moving the crystal translationally to produce the wavelengths listed previously.

The OPO output $< 1\,\text{mW}$ of $3.677\,\mu\text{m}$ light; however, this could be optimized by adjusting the input and output couplers. The idler and signal powers were unstable, and drifted over time. This power seemed to be most stable between fifteen minutes and an hour after the OPO was first turned on. When the power did drift, it could be reoptimized by adjusting these input and output couplers, which became more frequently-necessary the longer the OPO was in use.

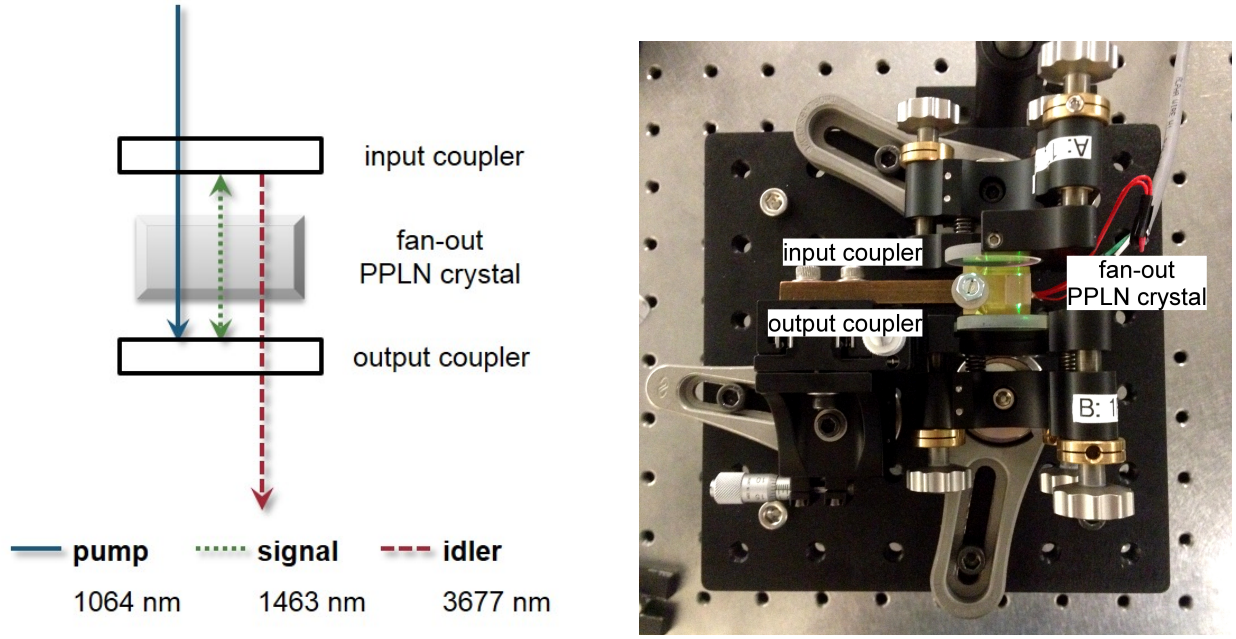

(a) OPO Diagram

(b) OPO Picture

Figure 14: Optical Parametric Oscillator Crystal

These figures focus on the design centered around the OPO crystal. Figure 14a clearly shows the schematic for the set-up, in which the input coupler transmits only $1\,\mu\text{m}$ pump light—reflecting the signal and idler—and the output coupler transmits only $3\,\mu\text{m}$ light—reflecting the pump and signal. Figure 14b is a picture of the set-up corresponding to this schematic, in which it is possible to see green light in the crystal.

Experimental Design

Again, it was important to ensure that all of the light incident on the sample was p-polarized. This was achieved for the measurement at 1.534 µm using a wave plate. However, another difficulty in working with 3.677 µm light, in addition to low power and limited detector options, was that polarization optics, such as the polarizing beam splitter used when making the bulk loss measurement for 1.534 µm light, are not easily accessible for light in the mid-infrared. Therefore, a periscope was constructed to change the s-polarized light emitted by the OPO into p-polarized light.

Figure 15 shows the schematic for the Brewster angle measurement set up. The germanium

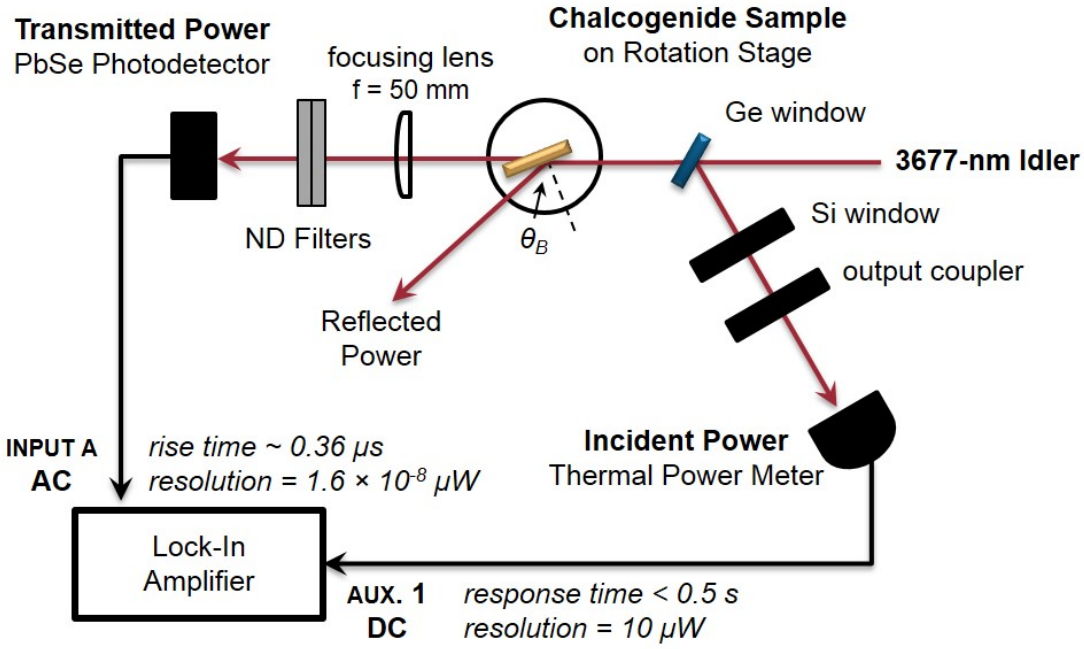

Figure 15: 3.677 µm Brewster Angle Measurement Set-Up Schematic

This figure shows the complete measurement set-up, including the OPO light source and filters, including a silicon window and an output coupler with the same specifications as that used in the OPO set-up (Figure 14), to ensure that only 3.677 µm light is incident on the sample and measured on the detectors. The chalcogenide sample is mounted on a rotation stage, which could be turned until the idler was incident on the sample at the Brewster angle, θ_B.

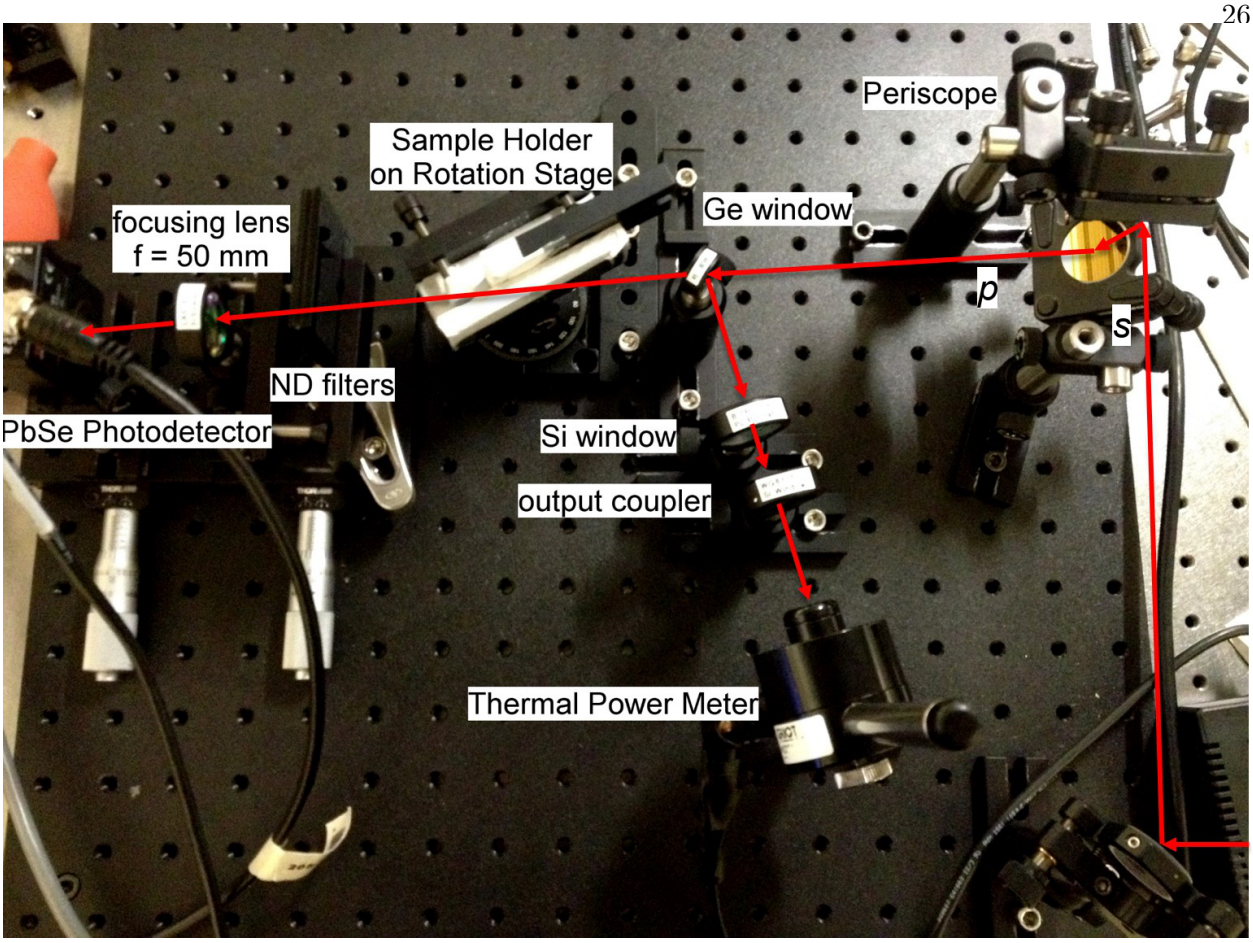

Figure 16: Mid-Infrared Brewster Angle Measurement Set-Up Picture

This is a picture of the set-up corresponding to the schematic shown in Figure 15. The periscope, which appears in this picture but is not shown in the schematic, is essential to the Brewster angle measurement; *s*-polarized light incident on the top mirror of the periscope was reflected onto the bottom mirror which reflects *p*-polarized light.

(Ge) window served two important purposes. It transmits 50 % 3.677 µm light and no pump, signal, or visible light, effectively filtering all but the idler and ensuring that only 3.677 µm light is incident on the sample [34]. This is important since this measurement was meant to measure the bulk loss at 3.677 µm. Secondly, the Ge window reflects some of the 3.677 µm light that it does not transmit, making it possible to monitor the power incident on the sample. This was necessary in order to measure the transmission $T = P_T/P_I$, used to calculate the bulk loss coefficient.

Transmittance Measurement

The PbSe detector is sensitive in the mid-infrared, and was used to measure the idler transmitted through the sample. The detector is very sensitive, so ND filters were necessary to ensure that the signal was not too strong to be measured by the detector. The lens was added before to focus the beam onto the detectors to ensure that all of power in the idler was measured. This detector outputs an AC signal which must be time-averaged before it could be used in a ratio calculation.

A Melles-Griot thermal power meter was chosen to monitor the incident power. Two additional filters were added to ensure that only the 3.677 µm light was detected by the power meter: a silicon window and an output coupler mirror. Each of these filters transmitted $> 98\,\%$ of the 3.677 µm light and reflected or absorbed all other light. Even though the Melles-Griot power meter is only sensitive to 0.01 mW, it has the advantage of a long calibration range from 20 nm to 20 µm [35]. The lock-in amplifier can read the AC signal from the PbSe detector and the DC signal The lock-in can then average the AC signal and return the ratio given in Equation 18a, where V_{PbSe} is the voltage output by the PbSe detector and V_{MG} is the voltage output by the Melles-Griot power meter.

$$R = \frac{V_{\mathrm{PbSe}}}{V_{\mathrm{MG}}} \tag{18a}$$

Although the OPO power drifted over time, the ratio of power measured by each detector was expected to be stable at all times. Two different ratio measurements were taken in order to calculate the transmittance through the chalcogenide sample. The monitored incident power can be related to the power incident on the sample by measuring the ratio of power R_{Ge} transmitted through and incident on the Ge window, without the sample in place, as seen in Figure 17a. Here, R_{Ge} is given by Equation 18b, where $V_{\mathrm{Ge,\,R}}$ and $V_{\mathrm{Ge,\,T}}$ are the measured voltages of the signals

incident upon and transmitted through the Ge window.

$$R_{\mathrm{Ge}} = \frac{V_{\mathrm{Ge,\ T}}}{V_{\mathrm{Ge,\ R}}} = \frac{V_{\mathrm{ChG,\ I}}}{V_{\mathrm{Ge,\ R}}} \tag{18b}$$

The transmitted signal, $V_{\mathrm{Ge,\ T}}$, is equivalent with that which will be incident upon the chalcogenide sample, $V_{\mathrm{ChG,\ I}}$, when it is added to the set-up. Figure 17b shows the set-up after the sample has been added. Now, R_{ChG} is given by Equation 18c, where $V_{\mathrm{ChG,\ I}}$ and $V_{\mathrm{ChG,\ T}}$ are the measured

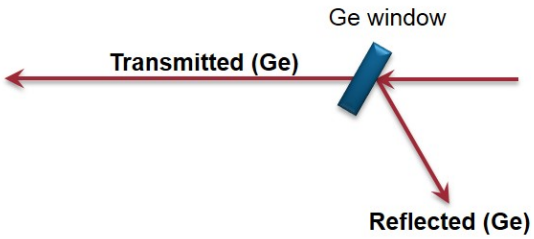

(a) Transmittance Diagram: Germanium Window

The ratio R_{Ge} was measured by recording the ratio of the signal $V_{\mathrm{Ge,\ T}}$ transmitted through the Ge window to the signal $V_{\mathrm{Ge,\ R}}$ reflected off of the window.

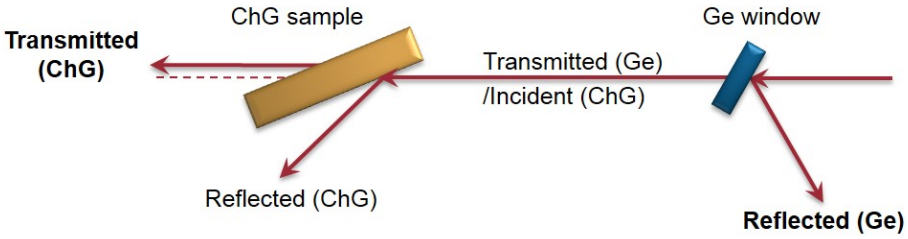

(b) Transmittance Diagram: Chalcogenide Sample

The ratio R_{ChG} was measured by recording the ratio of the signal $V_{\mathrm{ChG,\ T}}$ transmitted through the chalcogenide sample to the signal $V_{\mathrm{Ge,\ R}}$ reflected off of the germanium window.

Figure 17: Transmittance Diagrams

Each of these schematics depicts the method by which the ratios R_{Ge} and R_{ChG} (Equations 18b and 18c) can be measured by the lock-in amplifier as the ratio of the AC signal measured by the PbSe photodetector to the DC output of the thermal power meter (Equation 18a).

voltages of the signals incident upon and transmitted through the chalcogenide sample.

$$R_{\mathrm{ChG}} = \frac{V_{\mathrm{ChG,\ T}}}{V_{\mathrm{Ge,\ R}}} \tag{18c}$$

These ratios are then used to find the measured transmittance through the chalcogenide sample, T, necessary to compute the bulk loss coefficient.

$$T_{meas} = \frac{R_{\mathrm{ChG}}}{R_{\mathrm{Ge}}} = \frac{V_{\mathrm{ChG,\ T}}}{V_{\mathrm{ChG,\ I}}} \tag{18d}$$

Measurement Process

It is important to note that, now, the beam that will be measured by the PbSe detector shifts several mm when the sample is added. This is a result of the angle of transmittance $\theta_{TB} = \pi/2 - \theta_B$ inside the sample. Since the PbSe detector has an "active area" of only 2×2 mm, this shift is large enough to move the beam out of the area that can be seen by the detector. Both the focusing lens and photodetector were mounted on translation stages, which can be moved to optimize the signal measured by the photodetector.

Before the sample was mounted, it was important to determine the setting on the rotation stage at which the incident beam was normal to the sample. This was achieved by using a mirror that reflected the 1 µm and 1.5 µm light, some of which was still transmitted by the OPO output coupler. The rotation stage was then turned until the beam was reflected directly backward off of the mirror. The sample was then placed in the mount and turned until the 3.677 µm light was incident on the sample at the Brewster angle. The translation stages holding the PbSe detector and focusing lens were adjusted until the power read by the photodetector was optimized. Then, the ratio of power read by the PbSe detector to that read by the power meter, R_{Ge}, was recorded over approximately 90 s and saved using LabView. The sample was then quickly removed from the sample holder, the stage positions were reoptimized, and the ratio R_{ChG} was saved for 90 s. This was repeated several times for each sample.

Error Analysis

The expected uncertainty in the bulk loss can be estimated by performing the error analysis using the detector limitations as the uncertainties in the measured signals, as was done for the bulk loss in the mid-infrared in Chapter III. Although the ratios described in Equations 18b and 18c related voltages, it will be easier to estimate the uncertainty by examining ratios of power. Since these are ratios, the units should not matter and the results should be the same.

The power that a detector can measure with certainty is limited by its noise-equivalent power, which is the power at which the detector "measures" its own noise. The noise-equivalent power specifications, listed on the power meter and PbSe photodetector datasheets, are as follows [35, 36]:

$$NEP_{\mathrm{PbSe}} = 1.5 \times 10^{-13}\,\mathrm{mW}/\sqrt{\mathrm{Hz}}$$

$$NEP_{\mathrm{MG}} = 10\,\mu\mathrm{W}$$

For the thermal power meter, the uncertainty in power measured by the detector was estimated to be $\delta P_{\mathrm{MG}} = NEP_{\mathrm{MG}}$. NEP_{PbSe} has the units of $\mathrm{mW}/\sqrt{\mathrm{Hz}}$. This can be used to find the minimum power that can be measured by a photodetector, P_{min}, in mW, using Equation 19, where B is the photodetector's 3 dB frequency, R_{max} is the detector's maximum responsivity, and $R(3.677\,\mu\mathrm{m})$ is its responsivity at $3.677\,\mu\mathrm{m}$ [37].

$$P_{min} = \frac{NEP \cdot R_{max}}{R(3.677\,\mu\mathrm{m})}\sqrt{B} \tag{19}$$

The minimum measurable power was used to approximate the uncertainty in the power measured by the photodiode. Using $B = 10\,\mathrm{kHz}$, $R_{max} = 3000\,\mathrm{V/W}$, and $R(3.677\,\mu\mathrm{m}) \approx 2760\,\mathrm{V/W}$, $\delta P_{\mathrm{PbSe}} \approx 1.6 \times 10^{-11}\,\mathrm{mW}$ [36, 38].

Both the transmittance and bulk loss for the samples have already been estimated for both samples, using the values found online for the same samples, only manufactured by VITRON.

However, it would be helpful to have estimated expected signal values that will be measured by the photodetector and power meter for both the measurement of R_{Ge} and R_{ChG} (see Equations 18b and 18c). Although both detectors return voltages, the power and voltage should be proportional, so it should be reasonable to perform the error analysis by examining power. The OPO power incident on the sample was estimated to be $P_{\mathrm{OPO}} \approx 0.5\,\mathrm{mW}$. The sample transmition was estimated to be that at the Brewster angle, found using Equation 13b. Finally, transmission through the Ge window was approximated using data provided by Thorlabs [34]:

$$T_{\mathrm{Ge}} = 49.672\,41\,\% \qquad @ \approx 3676.422\,\mathrm{nm}$$

This is the specified transmission when the beam incident on the Ge window is normal to its surface. This is not true for the measurement set-up, but should be a reasonable estimate for the purpose of estimating the uncertainty in the measurement.

The expected powers necessary to compute the ratios R_{Ge} and R_{ChG}, found in Equations 18b and 18c as well as the uncertainties in incident and transmitted power δP_{I} and δP_{T} are given below:

$$P_{\mathrm{Ge,\,T}} = P_{\mathrm{OPO}} T_{\mathrm{Ge}} \qquad P_{\mathrm{ChG,\,T}} = P_{\mathrm{OPO}} T_{\max} T_{\mathrm{Ge}} \qquad \delta P_{\mathrm{T}} = \delta P_{\mathrm{PbSe}}$$

$$P_{\mathrm{Ge,\,R}} = P_{\mathrm{OPO}} \left(1 - T_{\mathrm{Ge}}\right) \qquad P_{\mathrm{ChG,\,I}} = P_{\mathrm{OPO}} \left(1 - T_{\mathrm{Ge}}\right) \qquad \delta P_{\mathrm{I}} = NEP_{\mathrm{MG}}$$

These ratios were used to compute the measured transmittance, T_{meas}, through the chalcogenide sample. Each time a ratio was taken, its uncertainty was estimated using Equation 24b in Appendix B. The exact θ_B was used in this calculation with $\delta\theta_B \approx 2^\circ$. This was chosen since every two degrees are marked on the rotation stage, making each measurement precise to $\pm 1^\circ$. Two different measurements must be taken: one to determine the rotation stage setting at which the incident beam is normal to the sample and another when turning the stage to the Brewster angle.

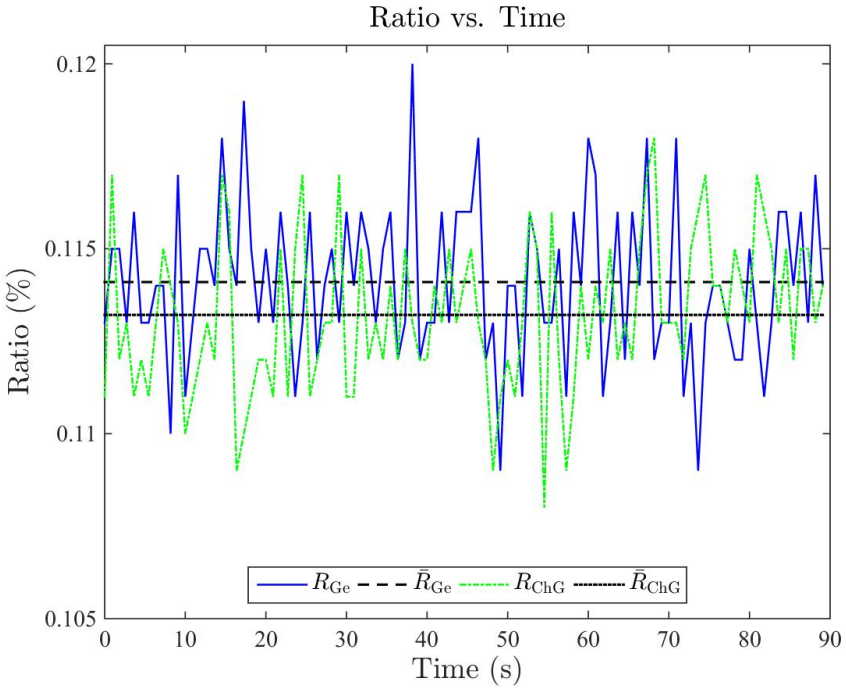

Figure 18: Ratio vs. Time for the $Ge_{33}As_{12}Se_{55}$ Sample

Multiple iterations of the measurement produced results resembling those in this plot. The averages are displayed on the plot, as well, with large error due to the fluctuating signals.

The uncertainty in bulk loss can be found using Equation 23, which becomes the expression given in Equation 20 since $\delta L \approx 0\,\mathrm{cm}$ is assumed.

$$\delta\alpha = \sqrt{\left(\frac{\cos\theta \ln T}{L}\right)^2 (\delta\theta)^2 + \left(\frac{\sin\theta}{LT}\right)^2 (\delta T)^2} \tag{20}$$

This results in the following estimated bulk loss coefficient:

$$\alpha \pm \delta\alpha \approx (0.05 \pm 0.13)\,\mathrm{cm}^{-1}$$

This large uncertainty means that the bulk loss coefficient will most-likely be an order-of-magnitude estimate rather than an exact and reliable value. This is seen in the signals measured on the lock-in amplifier. Figure 18, which shows the R_{ChG} and R_{Ge} ratios on the same plot. This supports the large estimated uncertainty in bulk loss. The average ratios $\bar{R}_{\mathrm{ChG}}$ and $\bar{R}_{\mathrm{Ge}}$ indicated on this plot

were used in calculating the bulk loss of the $Ge_{33}As_{12}Se_{55}$ sample. The results for both this and the $Ge_{28}Sb_{12}Se_{60}$ sample are discussed further in Chapter V.

CHAPTER V

RESULTS AND DISCUSSION

Calculated Bulk Loss at 1.534 µm

After careful measurement and error propagation, the following properties were measured for the two samples, $Ge_{33}As_{12}Se_{55}$ and $Ge_{28}Sb_{12}Se_{60}$:

Table 3: Bulk Loss at 1.534 µm

The measured values of the Brewster angle and bulk loss coefficients are summarized here for both $Ge_{28}Sb_{12}Se_{60}$ and $Ge_{33}As_{12}Se_{55}$. The expected values of bulk loss were calculated from the values of extinction coefficient, related to α by Equation 5, given on the Refractive Index Database. κ is listed with other relevant properties in Appendix A.

Property	Source	$Ge_{33}As_{12}Se_{55}$	$Ge_{28}Sb_{12}Se_{60}$
Brewster Angle θ_B	Theoretical	68.54°	69.40°
	Experimental	$(69.0 \pm 0.5)^\circ$	$(69.0 \pm 0.5)^\circ$
Bulk loss, α	Theoretical [39]	$0.0384 - 0.0576\,\mathrm{cm}^{-1}$	
	Expected [20, 21]	$0.036\,\mathrm{cm}^{-1}$	$0.059\,\mathrm{cm}^{-1}$
	Experimental	$(0.07 \pm 0.20)\,\mathrm{cm}^{-1}$	$(0.07 \pm 0.20)\,\mathrm{cm}^{-1}$

The $Ge_{33}As_{12}Se_{55}$ was used as a reference sample and was compared to results in measurements taken by Prasad et al. at 1.2 µm, which they reported was typically 2-3× lower at 1.5 µm [39]. The bulk loss coefficient measured for this sample was larger than what was predicted by the measurements at 1.2 µm; however, with the large uncertainty of $\pm 0.20\,\mathrm{cm}^{-1}$ for both the $Ge_{33}As_{12}Se_{55}$ and $Ge_{28}Sb_{12}Se_{60}$ samples, these measurements can be considered reasonable.

The largest source of uncertainty for this measurement came from the thermal power meters used to measure the power transmitted through and incident upon the sample. Several changes could be made to this measurement in order to improve the certainty in the measured values. Using more sensitive detectors, such as the InGaAs detectors used to measure the reflected power, to measure the transmitted and incident power as well could significantly reduce the uncertainty in these properties. This is especially promising for this measurement since the erbium fiber laser became relatively stable over time after the laser was stabilized by securing the fiber.

Calculated Bulk Loss at 3.677 µm

After many iterations of the Brewster angle measurement design, the bulk loss coefficient was measured for both the $Ge_{28}Sb_{12}Se_{60}$ sample and the $Ge_{33}As_{12}Se_{55}$ reference sample. These are listed in Table 4 along with the bulk loss coefficients predicted for the VITRON samples.

Several significant sources in error contributed to the large error in measuring the bulk loss coefficients of the $Ge_{28}Sb_{12}Se_{60}$ and $Ge_{33}As_{12}Se_{55}$ samples. Most significantly, the thermal power meter had a response time of < 0.5 s and a noise-equivalent power of 10 µW [35]. The slow response time is significant for this measurement technique, which involved averaging the ratios R_{Ge} and R_{ChG} over 90 s. The thermal power meter was most-likely unable to keep up with the faster and significantly more sensitive PbSe detector. For these reasons, it could be possible to reduce the uncertainty in this measurement by using another more sensitive detector, as was suggested for the measurement at 1.534 µm.

Table 4: Bulk Loss at 3.677 µm

The measured values of the Brewster angle and bulk loss coefficients are summarized here for both $Ge_{28}Sb_{12}Se_{60}$ and $Ge_{33}As_{12}Se_{55}$. The expected values of bulk loss were calculated from the values of extinction coefficient, related to α by Equation 5, given on the Refractive Index Database. κ is listed with other relevant properties in Appendix A.

Property	Source	$Ge_{33}As_{12}Se_{55}$	$Ge_{28}Sb_{12}Se_{60}$
Brewster Angle, θ_B	Theoretical [40, 19]	$68.54°$	$69.40°$
	Experimental	$(67.5 \pm 2.0)°$	$(71.5 \pm 2.0)°$
Bulk loss, α	Expected [20, 21]	$0.028\,\mathrm{cm}^{-1}$	$0.048\,\mathrm{cm}^{-1}$
	Experimental	$(0.03 \pm 0.16)\,\mathrm{cm}^{-1}$	$(0.06 \pm 0.18)\,\mathrm{cm}^{-1}$

Discussion and Future Work

Although the uncertainties in these measurements are very large, these results do answer the initial question: Can the $Ge_{33}As_{12}Se_{55}$ and $Ge_{28}Sb_{12}Se_{60}$ be considered transparent in the infrared? These values are of the order of magnitude predicted from the extinction coefficients and are supported by previous measurements by Prasad et al. [39]. These low values for the bulk loss coefficients support the claims of the chalcogenides' infrared transparency, showing promise for the future use of $Ge_{28}Sb_{12}Se_{60}$ as a low-loss waveguide for both the near- and mid-infrared.

It will be possible to improve these measurements and decrease the uncertainty in the bulk loss coefficient measurements by measuring all quantities with sensitive photodetectors. Although much more power was achieved using the erbium fiber laser than with the OPO, the uncertainty was similarly high, most-likely due to the detectors used in making the measurement. The thermal power meter was used to measure both the incident and transmitted power at 1.534 µm while the very sensitive InGaAs photodetector was used to measure the reflected power. However, since the reflected power was not measured at 3.677 µm or included in the calculation. The thermal power

meter was used to monitor the incident power, although indirectly, while the very sensitive GaAs detector was used to measure the transmitted power. Measuring the larger values, transmitted and incident power, with more sensitive detectors and bypassing the reflected power measurement altogether could help decrease the uncertainty in power both values of bulk loss, each at 1.534 µm and 3.677 µm. Making this improvement will increase confidence in the measured bulk loss values, making them better than order-of-magnitude approximations.

APPENDIX A

SAMPLE PROPERTIES

This Appendix summarizes every property of $Ge_{33}As_{12}Se_{55}$ and $Ge_{28}Sb_{12}Se_{60}$ referenced in calculations. The bulk loss was measured for SCHOTT IRG 22 and IRG 25; however, VITRON IG 2 and IG 5 were used for reference during method analysis. This was helpful since values were listed on RefractiveIndex.INFO for the extinction coefficients of VITRON IG 2 and IG 5 [20, 21]. These values could be used to compute the expected bulk loss coefficients for each of these samples using Equation 5.

The values for the sample diameter and thickness are listed on the sample packaging and do not have references listed in the tables below. All other properties were found on either the SCHOTT sample datasheets [41, 42] or the RefractiveIndex.INFO database [40, 19, 20, 21]. Two properties listed in the tables are not found in any of these sources: the Brewster angle and the bulk loss coefficient. Rather, the Brewster angle was calculated using Equation 8 and the bulk loss coefficient was calculated using Equation 5.

Table 5: SCHOTT IRG 22 and IRG 25 Properties

Property	$Ge_{33}As_{12}Se_{55}$ (IRG 22)	$Ge_{28}Sb_{12}Se_{60}$ (IRG 25)
Diameter, D	1 in	1 in
Thickness, L	0.2 cm	0.2 cm
Refractive index, n_0 [40, 19]		
@ 1534.29 nm	2.5444	2.6608
@ 3677.43 nm	2.5145	2.6235
Brewster angle, θ_B		
@ 1534.29 nm	68.544°	69.402°
@ 3677.43 nm	68.313°	69.136°
Material Properties [41, 42]		
Density, ρ	4.41 g/cm^3	4.66 g/cm^3
Specific heat, c_p	0.33 J/(g · K)	0.33 J/(g · K)
Thermal conductivity, k_{Th}	0.24 W/(m · K)	0.25 W/(m · K)

Table 6: VITRON IG 2 and IG 5 Properties

Property	$Ge_{33}As_{12}Se_{55}$ (IG 2)	$Ge_{28}Sb_{12}Se_{60}$ (IG 5)
Refractive index, n_0 [20, 21]		
@ 1534.29 nm	2.5445	2.6610
@ 3677.43 nm	2.5145	2.6237
Brewster angle, θ_B		
@ 1534.29 nm	68.545°	69.404°
@ 3677.43 nm	68.313°	69.136°
Extinction coefficient, κ [20, 21]		
@ 1534.29 nm	4.4343×10^{-7}	7.2622×10^{-7}
@ 3677.43 nm	8.1433×10^{-7}	1.4176×10^{-6}
Bulk loss coefficient, α		
@ 1534.29 nm	$0.036\,\mathrm{cm}^{-1}$	$0.059\,\mathrm{cm}^{-1}$
@ 3677.43 nm	$0.028\,\mathrm{cm}^{-1}$	$0.048\,\mathrm{cm}^{-1}$

APPENDIX B

ERROR ANALYSIS AND PROPAGATION

This Appendix provides an overview of the methods of error propagation used in analyzing data and determining the results of the bulk loss measurements in both the near- and mid-infrared. For N samples of a quantity x, with each sample labeled x_i, the standard deviation,σ_x, in that sample set can be found using Equation 21, where $\bar{x}$ is the mean value of all of the samples in that set.

$$\sigma_x = \sqrt{\frac{1}{N-1}\sum_{i=1}^{N}(x_i - \bar{x})^2} \tag{21}$$

For a function $f(x_1, \ldots, x_n)$ of n variables, the uncertainty, δf, in f is given by Equation 22, where $\delta x_1, \ldots, \delta x_n$ are the uncertainties in $x_1, \ldots, x_n$.

$$\delta f = \sqrt{\left(\frac{\partial f}{\partial x_1}\delta x_1\right)^2 + \cdots + \left(\frac{\partial f}{\partial x_n}\delta x_n\right)^2} \tag{22}$$

For the bulk loss coefficient, for example, Equation 22 becomes 23.

$$\delta\alpha = \sqrt{\left(\frac{\partial \alpha}{\partial \theta}\delta\theta\right)^2 + \left(\frac{\partial \alpha}{\partial T}\delta T\right)^2 + \left(\frac{\partial \alpha}{\partial L}\delta L\right)^2} \tag{23}$$

Another operation performed frequently during error analysis involves taking a ratio, such as $z = x/y$. In general, the uncertainty, δz, is given by Equation 24a, where δx and δy are the uncertainties

in x and y. This can be rewritten as Equation 24b.

$$\delta z = \sqrt{\left(\frac{\partial z}{\partial x}\delta x\right)^2 + \left(\frac{\partial z}{\partial y}\delta y\right)^2} \tag{24a}$$

$$\delta z = z\sqrt{\left(\frac{\delta x}{x}\right)^2 + \left(\frac{\delta y}{y}\right)^2} \tag{24b}$$

APPENDIX C

DISPERSION

Four factors contribute to the dispersion term, $F(x)$, which is referenced in Equation 4: two-photon absorption, Raman scattering, and the linear and quadratic Stark effects. Their individual contributions were derived by Sheik-Bahae et al. and are included in Table II of their paper [18]. They are included here as well for reference.

$$F_{\mathrm{2PA}}(x) = \frac{1}{(2x)^6}\left(-\frac{3x^2}{8}\frac{1}{(1-x)^{1/2}} + 3x\,(1-x)^{1/2} - 2\,(1-x)^{3/2} + 2\Theta\,(1-2x)\,(1-2x)^{3/2}\right) \tag{25a}$$

$$F_{\mathrm{RAM}}(x) = \frac{1}{(2x)^6}\left(-\frac{3x^2}{8}\frac{1}{(1+x)^{1/2}} - 3x\,(1+x)^{1/2} - 2\,(1+x)^{3/2} + 2\,(1+2x)^{3/2}\right) \tag{25b}$$

$$F_{\mathrm{LSE}}(x) = \frac{1}{(2x)^6}\left(2 - (1-x)^{3/2} - (1-x)^{3/2}\right) \tag{25c}$$

$$F_{\mathrm{QSE}}(x) = \frac{1}{(4x)^5}\left(\frac{1}{(1-x)^{1/2}} + \frac{1}{(1+x)^{1/2}} - \frac{x}{2}\frac{1}{(1-x)^{3/2}} - \frac{x}{2}\frac{1}{(1+x)^{3/2}}\right) \tag{25d}$$

A divergence term, given in Equation 26, is subtracted from the four main terms.

$$F_{\mathrm{DIV}}(x) = \frac{1}{(4x)^5}\Bigg(-2 - \frac{35x^2}{8} + \frac{x}{8}\frac{(3x-1)}{(1-x)^{1/2}} - 3x\,(1-x)^{1/2} + (1-x)^{3/2} \\ + \frac{x}{8}\frac{(3x+1)}{(1+x)^{1/2}} + 3x\,(1+x)^{1/2} + (1+x)^{3/2}\Bigg) \tag{26}$$

This is then normalized such that $\lim_{x\to 0} F(x) = 1$ to get the final dispersion term:

$$F(x) = \frac{65\,536}{917}\big(F_{2PA}(x) + F_{RAM}(x) + F_{LSE}(x) + F_{QSE}(x) - F_{DIV}(x)\big) \tag{27}$$

This was plotted in Figure 2a as a function of the ratio of the photon energy, $\hbar\omega$, to the optical gap E_g.

BIBLIOGRAPHY

[1] W. Park and J. Gopinath, "Slow Light Enhanced Mid-infrared Nonlinear Optical Devices," NSF EECS-1232077 (funded 2012).

[2] B. J. Eggleton, B. Luther-Davies, and K. Richardson, "Chalcogenide photonics," Nat. Photon. **5**, 141–148 (2011).

[3] A. B. Seddon, "Chalcogenide glasses: a review of their preparation, properties and applications," J. of Non-Cryst. Solids **184**(0), 44–50 (1995).

[4] M. R. Krogstad, S. Ahn, W. Park, and J. T. Gopinath, "Nonlinear characterization of $Ge_{28}Sb_{12}Se_{60}$ bulk and waveguide devices," Opt. Express **23**(6), 7870–7878 (2015).

[5] U. Willer, M. Saraji, A. Khorsandi, P. Geiser, and W. Schade, "Near- and mid-infrared laser monitoring of industrial processes, environment and security applications," Opt. and Lasers in Eng. **44**(7), 699–710 (2006).

[6] L. S. Rothman, D. Jacquemart, A. Barbe, et al., "The HITRAN 2004 molecular spectroscopic database," J. Quant. Spectrosc. Radiat. Transf. **96**(2), 139–204 (2005).

[7] J. Gopinath and W. Park, "Integrated nonlinear photonics platform for the mid-infrared," .

[8] M. Loudon, Organic Chemistry, 5th ed. (Roberts and Company Publishers, 2009).

[9] G. Lenz, J. Zimmermann, T. Katsufuji, et al., "Large Kerr effect in bulk Se-based chalcogenide glasses," Opt. Lett. **25**(4), 254–256 (2000).

[10] M. Asobe, T. Kanamori, and K. Kubodera, "Applications of highly nonlinear chalcogenide glass fibers in ultrafast all-optical switches," IEEE J. Quant. Electron. **29**(8), 2325–2333 (1993).

[11] M. El-Amraoui, J. Fatome, J. C. Jules, et al., "Strong infrared spectral broadening in low-loss As-S chalcogenide suspended core microstructured optical fibers," Opt. Express **18**(5), 4547–4556 (2010).

[12] F. Smektala, C. Quemard, L. Leneindre, et al., "Chalcogenide glasses with large non-linear refractive indices," J. Non-Cryst. Solids **239**(13), 139–142 (1998).

[13] D. J. Griffiths, Introduction to Electrodynamics, 3rd ed. (Prentice Hall, 1999).

[14] R. W. Boyd and G. L. Fischer, Encyclopedia of Materials: Science and Technology, chap. Nonlinear Optical Materials, pp. 6237–6244 (Elsevier, 2001).

[15] S. Doluweera, "The Role of Electric Polarization in Nonlinear optics," Tech. rep., University of Cincinnati (2001).

[16] R. W. Boyd, Nonlinear Optics, 3rd ed. (Elsevier, 2008).

[17] M. Dinu, F. Quochi, and H. Garcia, "Third-order nonlinearities in silicon at telecom wavelengths," Appl. Phys. Lett. **82**(18), 2954–2956 (2003).

[18] M. Sheik-Bahae, D. C. Hutchings, D. J. Hagan, and E. W. Van Stryland, "Dispersion of bound electron nonlinear refraction in solids," IEEE J. Quant. Electron. **27**(6), 1296–1309 (1991).

[19] M. N. Polyanskiy, "Optical constants of SCHOTT - IRG," (2014).

[20] M. N. Polyanskiy, "Optical constants of VITRON - IG," (2014).

[21] M. N. Polyanskiy, "Optical constants of VITRON - IG," (2014).

[22] M. Hass, J. W. Davisson, H. B. Rosenstock, and J. Babiskin, "Measurement of Very Low Absorption Coefficients by Laser Calorimetry," Appl. Opt. **14**(5), 1128–1130 (1975).

[23] H. B. Rosenstock, M. Hass, D. A. Gregory, and J. A. Harrington, "Analysis of laser calorimetric data," Appl. Opt. **16**(11), 2837–2842 (1977).

[24] D. A. Pinnow and T. C. Rich, "Development of a Calorimetric Method for Making Precision Optical Absorption Measurements," Appl. Opt. **12**(5), 984–992 (1973).

[25] K. Ogusu, K. Suzuki, and H. Nishio, "Simple and accurate measurement of the absorption coefficient of an absorbing plate by use of the Brewster angle," Opt. Lett. **31**(7) (2006).

[26] K. K. Sharma, Optics: Principles and Applications, 1st ed. (Academic Press, 2006).

[27] H. Liu, Z. Liu, E. S. Lamb, and F. Wise, "Self-similar erbium-doped fiber laser with large normal dispersion," Opt. Lett. **39**(4) (2014).

[28] R. C. Schardt, "Photodarkening of Germanium-Selenium Glasses Induced by Below-Bandgap Light," Ph.D. thesis, University of Florida (2000).

[29] M. Olivier, J. Tchahame, P. Němec, et al., "Structure, nonlinear properties, and photosensitivity of $(GeSe_2)_{100-x}(Sb_2Se_3)_x$ glasses," Opt. Mater. Express **4**(3), 525–540 (2014).

[30] S. A. Akhmanov, R. L. Byer, A. I. Kovrygin, A. P. Sukhorukov, and J. Warner, Quantum Electronics: A Treatise, vol. 1 (Academic Press Inc., 1975).

[31] M. H. Dunn and M. Ebrahimzadeh, "Parametric Generation of Tunable Light from Continuous-Wave to Femtosecond Pulses," Science **286**(5444), 1513–1517 (1999).

[32] R. Niederriter, "Idler wavelength range without signal," Tech. rep., University of Colorado (2013).

[33] S. Brosnan and R. L. Byer, "Optical parametric oscillator threshold and linewidth studies," IEEE J. Quant. Electron. **15**(6), 415–431 (1979).

[34] Thorlabs, WG90530 (Germanium transmission 1-4 microns) (2015).

[35] Melles-Griot, Integrated 2-Watt Broadband Power and Energy Meter System.

[36] Thorlabs, PDA20H PbSe Preamplified Detector (2014).

[37] Newport, "General Purpose Detector and Receiver FAQs," (2015).

[38] Thorlabs, PbS Amplified Photodetectors.

[39] A. Prasad, C.-J. Zha, R.-P. Wang, et al., "Properties of $Ge_xAs_ySe_{1-x-y}$ glasses for all-optical signal processing," Opt. Express **16**(4), 2804–2815 (2008).

[40] M. N. Polyanskiy, "Optical constants of SCHOTT - IRG," (2014).

[41] SCHOTT, Infrared Chalcogenide Glass IRG 22 (2013).

[42] SCHOTT, Infrared Chalcogenide Glass IRG 25 (2013).